Optimized-Pulse-Pattern Multistep Finite-Control-Set MPC With Real-Time Validation

Cristóbal González, *Student Member, IEEE*, Alejandro Angulo, *Member, IEEE*, and Fernando Mancilla-David, *Member, IEEE*

***Abstract*—This article addresses the main performance issues of multistep-finite-control-set model predictive control (MFCS-MPC) that make it impractical in medium-voltage high-power grid-connected converters. Current MFCS-MPC techniques synthesize nonperiodic steady-state voltages that produce harmonic-rich continuous and unpredictable Fourier spectra with variable switching frequency. This article leverages advances in optimized pulse patterns and MFCS-MPC to meet grid codes while operating at a low, fixed switching frequency and rendering a fast dynamic response. To keep the strategy viable in real time, enhancements to the sphere decoder algorithm that solves the optimization problem were made, and the computationally efficient Frank–Wolfe algorithm was used to find a new center for the sphere during transients. The control scheme is assessed through simulation and hardware-in-the-loop experiments, demonstrating its real-time viability.**

***Index Terms*—Grid-connected converters, model predictive control (MPC), multistep-finite-control-set (MFCS), optimized pulse patterns (OPPs).**

I. Introduction

GRID-CONNECTED power converters must comply with various requirements defined in technical standards [1], mostly related to the harmonic emission resulting from switching. In medium-voltage high-power (MVHP) applications, switching frequency is critical, as high-switching frequency leads to significant losses due to large nominal currents and high-blocking voltages [2].

Because of industry advances in the computing capacity of commercial control platforms, optimization-based control techniques such as model predictive control (MPC) have gained popularity over the last decade for multiobjective control problems [2], [3]. MPC has shown promising results regarding steady-state and dynamic performance, and with long prediction horizons, it can naturally deal with the oscillations of the LCL filters used in MVHP applications.

Nevertheless, the high overhead of solving the MPC optimization problem in real time is still an issue. In that line, multistep finite-control-set (MFCS) MPC has been proven to be executable in real time by commercial control platforms by solving the optimization problem through the sphere-decoder-algorithm (SDA) [2], [4]. However, the SDA overhead is still high during transient operation when the sphere's center location is away from the feasible set. This issue was solved effectively by dynamically modifying the center of the sphere [5]; however, an analysis of computational resources is still pending.

In addition, in steady state, MFCS-MPC does not generate periodic voltage waveforms nor three-phase-symmetrical voltages, resulting in continuous and unpredictable Fourier spectra and asymmetric losses between phases. Therefore, in its current form, MFCS-MPC approaches are unsuitable for grid-connected applications [6].

On the other hand, optimized pulse patterns (OPPs) are an excellent option for low and fixed switching frequency operation, as they optimize some system performance metrics while fixing the switching frequency [7]. On their own, OPPs yield a slow dynamic response but provide an excellent trade-off between harmonic distortion and switching frequency. To improve their dynamic response, previous works [8], [9], [10] have incorporated OPPs into an MPC scheme, resulting in a fast dynamic response and excellent steady-state performance. Regarding grid-connected applications, the incorporation of the LCL filter model in the OPP optimization problem [9] along with constraints over the amplitude of the grid currents harmonics has proved to be effective in meeting grid codes [11].

Controlling an LCL filter grid-connected MVHP converter poses a set of control objectives. On the one hand, long-term goals include minimizing the distortion of the grid currents, operating at a low and fixed switching frequency, and producing periodic and three-phase symmetrical voltages. On the other hand, short-term and general objectives must also be met, such as a fast dynamic response, a low computational burden, long prediction horizons to avoid additional elements such as active damping, and a simple control structure.

To deal with all these objectives, this article bridges OPPs with MFCS-MPC to address the weak spots of the latter, enhancing

Received 22 October 2024; revised 1 February 2025 and 7 April 2025; accepted 2 May 2025. Date of publication 14 May 2025; date of current version 30 June 2025. This work was supported in part by the National Agency for Research and Development (ANID) Chile through the Basal Project under Grant AFB240002, in part by the Advanced Center for Electrical and Electronic Engineering, AC3E, and in part by the UTFSM through projects under Grant PI_LIR_24_15 and Grant PIIC-006/2021. Recommended for publication by Associate Editor P. Karamanakos. *(Corresponding author: Alejandro Angulo.)*

Cristóbal González was with the Electrical Engineering Department, Universidad Técnica Federico Santa María, Valparaíso 2340000, Chile. He is now with the Electromechanics and Power Electronics Group, Department of Electrical Engineering, Eindhoven University of Technology, 5600MB Eindhoven, The Netherlands (e-mail: c.a.gonzalez.duguet@tue.nl).

Alejandro Angulo is with the Department of Electrical Engineering, Universidad Técnica Federico Santa María, Valparaíso 2340000, Chile (e-mail: alejandro.angulo@usm.cl).

Fernando Mancilla-David is with the Department of Electrical Engineering, University of Colorado Denver, Denver, CO 80204 USA (e-mail: fernando.mancilla-david@ucdenver.edu).

Color versions of one or more figures in this article are available at https://doi.org/10.1109/TPEL.2025.3570191.

Digital Object Identifier 10.1109/TPEL.2025.3570191

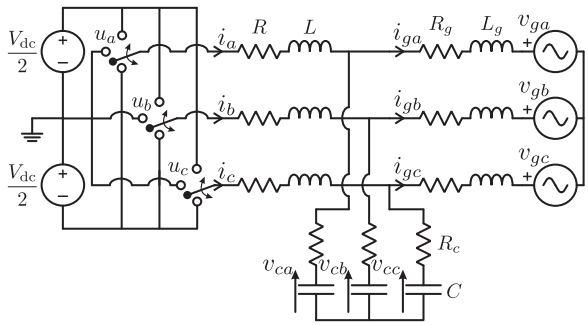

Fig. 1. Circuit schematic of the system under study.

its performance so it can be suitable for MVHP applications. Programmed patterns have been included into FCS-MPC before in [12], by sampling selective harmonic elimination patterns and adding them to the cost function as tracking references for the converter voltage. However, the concept of output trajectory tracking was not considered. A first exploration of this concept in the context of OPP-MFCS was performed by the authors of this article through a simple case study in [13], showing promising results. With the main objective of addressing performance issues of MFCS-MPC, this article formalizes and extends [13] for MVHP applications, and, very importantly, it proposes practical methods to improve the MFCS-MPC computational efficiency, verifying the strategy viability for real-time implementation during both steady-state and transient operation. This work also extends the MFCS-MPC formulation used in [13] to address the burst in switching frequency during transients, introducing a constraint that adds an additional degree of flexibility to alleviate this issue.

The contributions of this article are the following.

1) An MPC strategy that addresses the main performance issues of MFCS-MPC in grid-connected MVHP applications by leveraging its features with those of OPPs.
2) It proposes and validates a generalized exploration pattern for the SDA, improving its computational efficiency at no additional computation cost and leaving more computation time for additional elements.
3) It implements and verifies the real-time viability of the Frank–Wolfe algorithm (FWA) to obtain a new sphere center for the SDA, ensuring it is viable in real time during transient operation.

The rest of this article is organized as follows. Section II presents the model of the system and control objectives, Section III describes each element of the proposed control strategy, Section IV details the main contributions in MFCS-MPC efficiency, Section V presents simulation results, whereas Section VI validates the strategy via high-level synthesis (HLS) and hardware-in-the-loop (HIL) results. Finally, Section VII concludes this article.

II. System Under Study

A. Mathematical Model

The analyzed system is an LCL filter grid-connected three-level neutral point clamped (3L-NPC) converter, as shown in Fig. 1, which is a widely used architecture for MVHP applications. Consider a grid with angular frequency ω_g, rated apparent power S_{nom}, rated line-to-line rms voltage V_g, and rated rms current I_{nom}. The continuous-time model of the system, in per unit (p.u.) (with base values the peak rated current and peak phase voltage of the grid), is

$$\begin{aligned}\dot{\boldsymbol{x}}(t) &= \boldsymbol{F}\boldsymbol{x}(t) + \boldsymbol{G}\boldsymbol{P}\boldsymbol{u}_{abc}(t)\\ \boldsymbol{y}(t) &= \boldsymbol{C}\boldsymbol{x}(t)\end{aligned} \tag{1}$$

where

$$\boldsymbol{F} = \omega_g \begin{bmatrix} -\frac{R+R_c}{L}\boldsymbol{I}_2 & \frac{R_c}{L}\boldsymbol{I}_2 & -\frac{1}{L}\boldsymbol{I}_2 & \boldsymbol{0}_2 \\ \frac{R_c}{L_g}\boldsymbol{I}_2 & -\frac{R_g+R_c}{L_g}\boldsymbol{I}_2 & \frac{1}{L_g}\boldsymbol{I}_2 & -\frac{1}{L_g}\boldsymbol{I}_2 \\ \frac{1}{C}\boldsymbol{I}_2 & -\frac{1}{C}\boldsymbol{I}_2 & \boldsymbol{0}_2 & \boldsymbol{0}_2 \\ \boldsymbol{0}_2 & \boldsymbol{0}_2 & \boldsymbol{0}_2 & \boldsymbol{M}_g \end{bmatrix}$$

$$\boldsymbol{G} = \frac{V_{\text{dc}}\omega_g}{2V_B}\begin{bmatrix}\frac{1}{L}\boldsymbol{I}_2 \\ \boldsymbol{0}_{6\times 2}\end{bmatrix} \quad \boldsymbol{C} = \begin{bmatrix}\boldsymbol{I}_6 \\ \boldsymbol{0}_{6\times 2}\end{bmatrix}^\top \quad \boldsymbol{M}_g = \begin{bmatrix}0 & -1 \\ 1 & 0\end{bmatrix}$$

and $\boldsymbol{\xi}_{abc} = [\xi_a\ \xi_b\ \xi_c]^\top$, $\boldsymbol{\xi}_{\alpha\beta} = [\xi_\alpha\ \xi_\beta]^\top$, $\boldsymbol{\xi}_{\alpha\beta} = \boldsymbol{P}\boldsymbol{\xi}_{abc}$, and $\boldsymbol{P}$ is the well-known Clarke's transformation matrix. The state-space vector is defined as $\boldsymbol{x} = [\boldsymbol{i}_{\alpha\beta}^\top\ \boldsymbol{i}_{g,\alpha\beta}^\top\ \boldsymbol{v}_{c,\alpha\beta}^\top\ \boldsymbol{v}_{g,\alpha\beta}^\top]^\top$, with the grid voltage included as an oscillator, and the input vector $\boldsymbol{u}_{abc} \in \boldsymbol{\mathcal{U}}$ comprising the converter's equivalent switches and $\boldsymbol{\mathcal{U}} \triangleq \mathcal{U}\times\mathcal{U}\times\mathcal{U}$ with $\mathcal{U} := \{-1, 0, 1\}$. Finally, the output vector is defined as $\boldsymbol{y} = [\boldsymbol{i}_{\alpha\beta}^\top\ \boldsymbol{i}_{g,\alpha\beta}^\top\ \boldsymbol{v}_{c,\alpha\beta}^\top]^\top$, $\boldsymbol{I}_n$ is the identity matrix of order n, $\boldsymbol{0}_{n\times m}$ is an n by m zero matrix, and $\boldsymbol{0}_n$ is a square zero matrix of order n. Through exact discretization, based on a sampling period T_s, the discrete-time model becomes

$$\begin{aligned}\boldsymbol{x}(k+1) &= \boldsymbol{A}\boldsymbol{x}(k) + \boldsymbol{B}\boldsymbol{u}_{abc}(k)\\ \boldsymbol{y}(k) &= \boldsymbol{C}\boldsymbol{x}(k)\end{aligned} \tag{2}$$

where $\boldsymbol{A} = e^{\boldsymbol{F}T_s}$ and $\boldsymbol{B} = -\boldsymbol{F}^{-1}(\boldsymbol{I}_8 - \boldsymbol{A})\boldsymbol{G}\boldsymbol{P}$.

B. Control Objectives

The type of grid code analyzed in this work poses limits on specific harmonics of the grid currents and on the total demand distortion (TDD) [1]. Together with meeting grid codes, the system operation must be efficient by reducing thermal losses, and safe, by preventing overheating of the semiconductors and having a fast dynamic response when needed. Hence, in steady state, the semiconductors must operate at a fixed and low switching frequency, generating periodic and three-phase-symmetrical voltages to obtain discrete Fourier spectra and symmetrical losses between phases. At the same time, the grid currents must meet grid codes (TDD and harmonics). Finally, it is also mandatory to track the grid's active and reactive power references precisely and with a fast dynamic response.

All the objectives besides the last one involve steady-state metrics. These metrics, such as switching frequency, TDD, and general grid code harmonic requirements, can be adjusted appropriately, can be adjusted appropriately with offline calculated patterns such as OPPs. However, on their own, OPPs generate a slow dynamic response. On the other hand, MFCS-MPC is viable in real time and provides a fast dynamic response with excellent reference tracking. To meet all control objectives

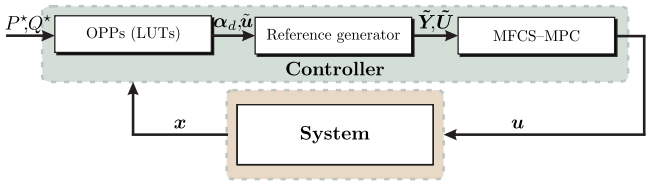

Fig. 2. Block diagram of the proposed control strategy.

simultaneously, the proposed strategy (OPP-MFCS) integrates both OPPs and MFCS-MPC in the control scheme detailed in the following section.

III. Control Scheme

The proposed control scheme is depicted in Fig. 2. In general terms, it consists in storing the OPPs in look-up-tables (LUTs) so a reference generator can use them to calculate, in real time, the trajectories that the system would follow in steady state if the system operates with the corresponding OPP. These trajectories are then used by the MFCS-MPC controller as references. The details regarding the proposed control structure are given in the following sections.

A. Optimized Pulse Patterns

This section gives a brief description of the OPPs used in this work. The reader is referred to [7] for a detailed mathematical model of OPPs. In general terms, OPPs $u(\theta)$ are periodic voltage waveforms designed for steady-state operation, consisting of a sequence of voltage steps at specific angular positions called switching angles (SAs). For simplicity, this work considers patterns with half and quarter-wave symmetry, with only positive values in the first half-wave (unipolar pattern). However, more generalized formulations, such as those in [7], may also be considered. Because of the symmetry, the pattern is fully described by its definition in the interval $[0, \frac{\pi}{2}]$, where d is the number of switching transitions in a quarter-wave. Moreover, even harmonics are zero, and the remaining harmonics have only sine part. Only the fundamental and harmonics of order $h = 6j \pm 1$ with $j \in \mathbb{Z}_{>0}$ can produce currents.

Let $\mathcal{H}$ be the set of cardinality H comprising the order of all consecutive harmonics that satisfy this condition, starting with $h = 5$, i.e., $\mathcal{H} = \{5, 7, 11, \dots\}$. To include grid codes, namely the IEEE Std. 519-2022 [1], the approach detailed in [11] was followed. To use the OPPs in the control strategy, the SAs ($\boldsymbol{\alpha}_d$) and the harmonic content of the pattern ($\tilde{\boldsymbol{u}}$), i.e., the signed amplitude of the sine part of each harmonic $h \in \mathcal{H}$, are stored in LUTs indexed by the modulation index m.

B. Multistep-Finite-Control-Set MPC

The variable-step-size formulation utilized here is based on a recent conference paper drafted by the authors [14]. The step size of the N steps in the prediction horizon is equal to the control period T_s scaled by the elements in the set $\mathcal{S} := \{s_1, s_2, \dots, s_N\}$, so the step sizes can differ from each other across the horizon, taking the values $T_s s_1, T_s s_2, \dots, T_s s_N$.

In every control period k, the behavior of the system is predicted for instants $k+1$ to $k+N$. The vector comprising the predicted outputs is defined as $\boldsymbol{Y}(k) = [\boldsymbol{y}^\top(k+1) \dots \boldsymbol{y}^\top(k+N)]^\top$, while the predicted control actions are ordered in the vector $\boldsymbol{U}(k) = [\boldsymbol{u}_{abc}^\top(k) \dots \boldsymbol{u}_{abc}^\top(k+N-1)]^\top$. In the traditional approach, the MFCS problem aims to track ideal references $\boldsymbol{Y}^\star(k)$ (defined as $\boldsymbol{Y}(k)$), whereas in the proposed strategy, the objective is to track the optimal trajectories that the system would follow in steady state when operating with OPPs. The trajectories $\tilde{\boldsymbol{Y}}(k)$ and the OPP sampled along the prediction horizon $\tilde{\boldsymbol{U}}(k)$ are obtained from the reference generator, leading to the proposed formulation of the MFCS-MPC problem:

$$\min_{\boldsymbol{U}(k)} J = \sum_{\ell=k+1}^{k+N} \|\Delta\tilde{\boldsymbol{y}}(\ell)\|^2_{\boldsymbol{\lambda}_\ell^y} + \sum_{\ell=k}^{k+N-1} \|\Delta\tilde{\boldsymbol{u}}_{abc}(\ell)\|^2_{\boldsymbol{\lambda}_\ell^u}$$

s.t.

$$\boldsymbol{x}(\ell+1) = \boldsymbol{A}_\ell \boldsymbol{x}(\ell) + \boldsymbol{B}_\ell \boldsymbol{u}_{abc}(\ell) \quad \forall \ell \in \mathcal{K}_{0:N-1} \tag{3a}$$

$$\boldsymbol{y}(\ell) = \boldsymbol{C}\boldsymbol{x}(\ell) \quad \forall \ell \in \mathcal{K}_{1:N} \tag{3b}$$

$$\boldsymbol{x}(k) = \boldsymbol{x}_0 \tag{3c}$$

$$\|\Delta\boldsymbol{u}_{abc}(\ell)\|_\infty \leq 1 \quad \forall \ell \in \mathcal{K}_{0:N-1} \tag{3d}$$

$$\sum_{\ell=k}^{k+N-1} \|\Delta u_\chi(\ell)\|_1 \leq \hat{c}_\chi(k) \quad \forall \chi \in \{a, b, c\} \tag{3e}$$

$$\boldsymbol{U}(k) \in \mathbb{U} \tag{3f}$$

where (2) is included as constraints, and because of the variable-step-size formulation, matrices $\boldsymbol{A}_\ell$ and $\boldsymbol{B}_\ell$ depend on ℓ. The weighted norms in the cost function are adjusted by the weighting factor matrices $\boldsymbol{\lambda}_\ell^y$ and $\boldsymbol{\lambda}_\ell^u$. The initial condition $\boldsymbol{x}_0$ is the vector of measured states at instant k, while $\mathcal{K}_{\eta:\xi} = \{k+\eta, \dots, k+\xi\}$ with $\eta < \xi$. The L-infinity norm is defined as $\|\boldsymbol{\varepsilon}\|_\infty := \max_i |\boldsymbol{\varepsilon}_i|$, and $\Delta\boldsymbol{u}_{abc}(\ell) = \boldsymbol{u}_{abc}(\ell) - \boldsymbol{u}_{abc}(\ell-1)$, so (3d) is imposed to limit the amplitude of the transitions in the converter voltage. The L1 norm is defined as $\|\boldsymbol{\varepsilon}\|_1 := \sum_i |\boldsymbol{\varepsilon}_i|$, and $\Delta u_\chi(\ell) = u_\chi(\ell) - u_\chi(\ell-1)$, so (3e) is a constraint added to prevent an excessive number of additional switching transitions during transients, on a per phase basis, with $\hat{c}_\chi(k)$ forcing a limit over the total predicted commutations. Finally, $\mathbb{U} \triangleq \boldsymbol{\mathcal{U}} \times \dots \times \boldsymbol{\mathcal{U}}$ is the N-times cartesian product of $\boldsymbol{\mathcal{U}}$. The cost function J defines the objectives of tracking the optimal trajectories and the sampled OPP, where $\Delta\tilde{\boldsymbol{y}}(\ell) = \tilde{\boldsymbol{y}}(\ell) - \boldsymbol{y}(\ell)$ and $\Delta\tilde{\boldsymbol{u}}_{abc}(\ell) = \tilde{\boldsymbol{u}}_{abc}(\ell) - \boldsymbol{u}_{abc}(\ell)$, with $\tilde{\boldsymbol{u}}_{abc}(\ell)$ being tracked in a similar way as in [12]. Through the procedure detailed in [4], problem (3) can be written as

$$\min_{\boldsymbol{U}(k)} \quad J = \|\boldsymbol{H}\boldsymbol{U}(k) - \bar{\boldsymbol{U}}_{\text{unc}}(k)\|_2^2$$
$$\text{s.t. (3d), (3e), and (3f)} \tag{4}$$

where all constraints besides (3d), (3e), and (3f) are part of the cost function, $\boldsymbol{U}_{\text{unc}}$ is the unconstrained solution of the problem, $\boldsymbol{H}$ is a transformation lower-triangular matrix called lattice generator, and $\bar{\boldsymbol{U}}_{\text{unc}} = \boldsymbol{H}\boldsymbol{U}_{\text{unc}}$. The reader is referred to [14] for further details.

Regarding the extension of the traditional MFCS-MPC formulation by introducing constraint (3e), it is pointed out that a constraint with such structure can be written in different forms and adds a degree of flexibility to (3). First, the parameter $\hat{c}_\chi(k)$ can be defined according to different criteria. Since it can be adjusted on each control step, it can, for example, be set depending on the number of commutations that have occurred in the previous N_{past} steps before k. In that way, $\hat{c}_\chi(k)$ would set the upper bound of the commutations in a time window of $N_{\text{past}} + N$ steps. On the other hand, it is also possible to define $\hat{c}_\chi(k) = c_{\tilde{u},\chi} + |\tilde{u}_\chi(k) - u_\chi(k-1)|$, where $c_{\tilde{u},\chi}$ is the number of switching transitions of the sampled OPP, in phase χ, along the prediction horizon, while $\tilde{u}_\chi(k)$ is the switching position of the OPP at instant k in phase χ. This allows that during transients, the converter can switch at least as many times as the sampled OPP, plus the number of commutations needed to go from $u_\chi(k-1)$ to $\tilde{u}_\chi(k)$. Such a definition of $\hat{c}_\chi(k)$ also guarantees that the original OPP always complies with (3e). Moreover, a simpler version of this constraint, such as

$$\sum_{\ell=k}^{k+N-1} \|\boldsymbol{u}_{abc}(\ell) - \boldsymbol{u}_{abc}(\ell-1)\|_1 \leq \hat{c} \tag{5}$$

that encompasses all three phases simultaneously and uses a constant bound is also an option. There are many ways of implementing a constraint over the switching transitions of the converter. However, this analysis is out of the work's scope and is suggested as future work.

C. Reference Generator

This entity calculates $\tilde{\boldsymbol{Y}}$ and $\tilde{\boldsymbol{U}}$ in real time using the information from the OPPs. The tracking references $\tilde{\boldsymbol{Y}}$ are the trajectories the system's outputs would follow in steady state when operating with the corresponding OPPs. On the other hand, $\tilde{\boldsymbol{U}}$ is the pattern sampled along the prediction horizon, hence, its generation is straightforward.

The output trajectory in the first step of the prediction horizon is $\tilde{\boldsymbol{y}}(\ell{=}k+1) = \tilde{\boldsymbol{y}}(\theta_1{=}\theta_{\text{PLL}} + s_1\omega_g T_s)$, where θ_{PLL} is the angular position reference calculated by a phase-locked-loop (PLL). Since $\tilde{\boldsymbol{y}}(\theta_1)$ is part of a steady-state trajectory resulting from periodic inputs (the OPPs), it can be found using Fourier series and phasor theory. Consider a set $\mathcal{H}_r$ that is the subset of $\mathcal{H}$ comprising the first H_r elements of $\mathcal{H}$, and that those H_r harmonic components of the OPPs are stored for each modulation index. Recall that the OPPs' harmonics only have a sine part, so only the signed amplitude is needed to store each harmonic. Therefore, the harmonic part in the trajectory of a generic output $\boldsymbol{w}_{\alpha\beta}$ can be determined as

$$\tilde{\boldsymbol{w}}^H_{\alpha\beta}(\theta_1) = \boldsymbol{P} \sum_{h\in\mathcal{H}_r} |\mathbf{W}^h| \begin{bmatrix} \sin\left(\theta_1 h + \angle\mathbf{W}^h\right) \\ \sin\left(\theta_1 h + \angle\mathbf{W}^h + \frac{4\pi h}{3}\right) \\ \sin\left(\theta_1 h + \angle\mathbf{W}^h + \frac{2\pi h}{3}\right) \end{bmatrix} \tag{6}$$

where $\mathbf{W}^h$ is the phasor of the hth harmonic of the output $\boldsymbol{w}$, calculated using phasor theory. Consequently, the trajectories to be followed in the first step of the prediction horizon are $\tilde{\boldsymbol{y}}(\theta_1) = [(\tilde{\boldsymbol{i}}_{\alpha\beta}(\theta_1))^\top, (\tilde{\boldsymbol{i}}_{g,\alpha\beta}(\theta_1))^\top, (\tilde{\boldsymbol{v}}_{c,\alpha\beta}(\theta_1))^\top]^\top$, where $\tilde{\boldsymbol{w}}_{\alpha\beta}(\theta_1) = \boldsymbol{w}^\star_{\alpha\beta}(\theta_1) + \tilde{\boldsymbol{w}}^H_{\alpha\beta}(\theta_1)$. Recall that the fundamental component in the trajectory of an output $\boldsymbol{w}_{\alpha\beta}$ is equal to the ideal reference $\boldsymbol{w}^\star_{\alpha\beta}$.

To determine the tracking references for the rest of the prediction horizon, the following model is used:

$$\tilde{\boldsymbol{Y}}_r = \boldsymbol{\Gamma}_r \tilde{\boldsymbol{x}}(\theta_1) + \boldsymbol{\Upsilon}_r \tilde{\boldsymbol{U}}_{[4:3N]} \tag{7}$$

where $\tilde{\boldsymbol{x}}(\theta_1)$ has the same elements as $\tilde{\boldsymbol{y}}(\theta_1)$, and also includes the grid voltage $\boldsymbol{v}_{g,\alpha\beta}(\theta_1)$, and the matrices $\boldsymbol{\Upsilon}_r$ and $\boldsymbol{\Gamma}_r$ are

$$\boldsymbol{\Upsilon}_r = \begin{bmatrix} \boldsymbol{C}\boldsymbol{B}_2 & & & \\ \boldsymbol{C}\boldsymbol{A}_3\boldsymbol{B}_2 & \boldsymbol{C}\boldsymbol{B}_3 & & \\ \vdots & \vdots & \ddots & \\ \boldsymbol{C}\left(\prod_{\ell=N}^{\ell=3}\boldsymbol{A}_\ell\right)\boldsymbol{B}_2 & \boldsymbol{C}\left(\prod_{\ell=N}^{\ell=4}\boldsymbol{A}_\ell\right)\boldsymbol{B}_3 & \cdots & \boldsymbol{C}\boldsymbol{B}_N \end{bmatrix}$$

$$\boldsymbol{\Gamma}_r = \begin{bmatrix} (\boldsymbol{C}\boldsymbol{A}_2)^\top & (\boldsymbol{C}\boldsymbol{A}_3\boldsymbol{A}_2)^\top & \cdots & \left(\boldsymbol{C}\prod_{\ell=N}^{\ell=2}\boldsymbol{A}_\ell\right)^\top \end{bmatrix}^\top.$$

Note that $\boldsymbol{\Upsilon}_r$ is a submatrix of the standard matrix $\boldsymbol{\Upsilon}$ in [14], so it is not necessary to calculate it again. Hence, the tracking references are determined as

$$\tilde{\boldsymbol{Y}}(k) = \begin{bmatrix} \tilde{\boldsymbol{y}}^\top(\theta_1) & \tilde{\boldsymbol{Y}}_r^\top \end{bmatrix}^\top. \tag{8}$$

Notice that $\tilde{\boldsymbol{Y}}_r$ is obtained by using $\tilde{\boldsymbol{U}}$ as the input in (7), which is generated by sampling the OPP using zero-order-hold with the sampling periods along the prediction horizon defined by $\mathcal{S}$. This means that $\tilde{\boldsymbol{U}}$ is not identical to the respective OPP; therefore, $\tilde{\boldsymbol{Y}}_r$ is not the exact steady-state trajectory. However, these are good approximations when the step sizes considered in the variable-step-size prediction horizon are small.

IV. Efficient Implementation of MFCS-MPC

This section presents the two contributions that enhance the efficiency of the SDA and its viability in real time.

A. Generalized SDA Exploration Pattern

This section assumes that the reader is familiarized with the SDA [15].

Consider a converter with output voltage levels going from $-\eta$ to η (e.g., for a 3L-NPC, $\eta = 1$, and the levels are $[-1, 0, 1]$, or $[\ominus, \text{⓪}, \oplus]$). The whole set $\mathbb{U}$ is organized in a search-tree, structured using the conventional approach as shown in Fig. 3(a). In this case, the exploration of each level j starts with the node $u_j = -\eta$ (understood as exploring the tree from left to right when using this tree arrangement). In Fig. 3(a), the first explored candidate is marked in red, and the initial solution, located anywhere in the tree, is marked in green.

The SDA initial candidate is always feasible and is chosen to render a small cost function value. Hence, instead of arbitrarily starting the exploration of the tree, it is proposed to first explore the zones of the tree that are close to the initial solution. This exploration pattern can be understood as a rearrangement of the search tree's elements while maintaining the original left-to-right exploration pattern; as a result, the first explored path is the initial solution.

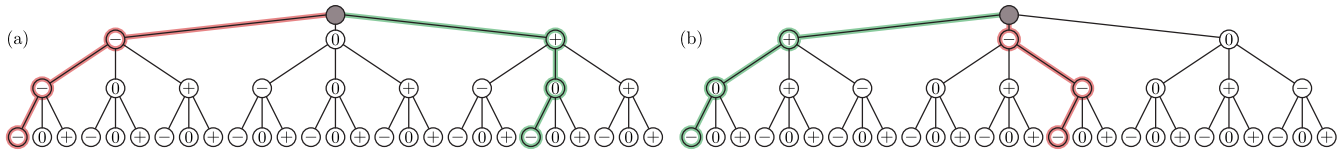

Fig. 3. Exploration of the search trees by the SDA. (a) Conventional exploration pattern. (b) Proposed rearrangement.

Understanding this proposed pattern as a rearrangement of the tree allows its representation as shown in Fig. 3(b), where the first explored path is the initial solution. The arrangement modifies the order of the nodes at each level. It places the corresponding entry in the initial solution as the first node on the left, while the rest can be sorted arbitrarily. In this case, for simplicity, and only to illustrate the working principle, a circular shift was used, so all the nodes initially located to the left of the corresponding entry are positioned at the extreme right in the same order. For example, if the initial solution entry is of type $\oplus$, the level is sorted from left to right as $[\oplus, \ominus, \textcircled{0}]$. To incorporate this exploration pattern into the traditional SDA, an array $\boldsymbol{O}_{\text{ep}}$ containing the order of each level is added as an input. This addition allows sorting each level as desired, providing the flexibility to define the tree arrangement based on any chosen criteria, enabling easy implementation of any convenient search pattern [16], [17]. Note that defining the best searching pattern is out of the scope of this work, and a circular shift is used only for illustrative purposes.

Incorporating $\boldsymbol{O}_{\text{ep}}$ as an input in the SDA only requires a few modifications and does not increase the SDA computational cost. Notice that this modification to the SDA is applicable to any η, making it suitable for any multilevel converter. It is important to highlight that, due to the proposed exploration pattern, the first explored path is always that of the initial candidate, which is perfectly known before starting the exploration. This differs significantly from the traditional approach, where the cost function of the full-depth path of the initial candidate is known before starting the exploration. The traditional SDA does not exploit this initial information, and during its execution, it goes from left to right, where it can eventually reach the initial candidate's path and reevaluate it according to its feasibility, unless a better candidate is found before.

With the proposed exploration pattern, the SDA can start directly at the end of the path, reducing the nodes explored by $3N$, as shown in [16]. Finally, the parallelization method presented in [18] can be incorporated by dividing the tree so each parallel SDA explores a subtree following its own exploration pattern. To illustrate the effectiveness of this rearrangement, numerical results are presented in Section V-A.

B. Transient Operation: The FWA

The SDA searches for potential candidates inside a sphere, where the initial radius depends on the location of its center $\bar{\boldsymbol{U}}_{\text{unc}}$ and the initial incumbent. Let $\mathbb{C}_{\mathbb{U}}$ be the convex hull of $\mathbb{U}$. Whenever $\boldsymbol{U}_{\text{unc}}$ is located far from $\mathbb{C}_{\mathbb{U}}$, the initial radius will be large. As detailed in [5], this frequently happens during transient operation. In such cases, regardless of the initial incumbent, the number of candidates inside the sphere will be large as all points in $\mathbb{C}_{\mathbb{U}}$ are far from $\boldsymbol{U}_{\text{unc}}$.

This work adopts the strategy used in [5] to deal with this issue. It consists in modifying the cost function of (4) every time $\boldsymbol{U}_{\text{unc}}$ is far from $\mathbb{C}_{\mathbb{U}}$, which primarily occurs during transient operation. In these cases, the cost function considered is

$$J_{\text{mod}} = \|\boldsymbol{H}\boldsymbol{U}(k) - \bar{\boldsymbol{U}}_{\text{bc}}(k)\|_2^2 \tag{9}$$

where J_{mod} is an approximation of the original cost function J, in which $\bar{\boldsymbol{U}}_{\text{unc}}$ (the center of the sphere) is replaced by $\bar{\boldsymbol{U}}_{\text{bc}} = \boldsymbol{H}\boldsymbol{U}_{\text{bc}}$, and $\boldsymbol{U}_{\text{bc}}$ is the euclidean projection of $\boldsymbol{U}_{\text{unc}}$ over $\mathbb{C}_{\mathbb{U}}$, which is obtained by solving the following box-constrained quadratic programming problem:

$$\min_{\boldsymbol{U}(k)\in\mathbb{C}_{\mathbb{U}}} \quad J = \boldsymbol{U}(k)^{\top}\boldsymbol{Q}\boldsymbol{U}(k) + 2\boldsymbol{\Theta}^{\top}\boldsymbol{U}(k). \tag{10}$$

An efficient solver for (10) is required, as most of the available computation time must be reserved for the SDA to find the optimal actuation. Although [5] used an exterior-point active-set-method (EP-ASM) to solve the problem, its computational feasibility on a commercial platform was not verified and is still a pending issue. Moreover, EP-ASMs do not guarantee strictly descent iterations [19], meaning that the algorithm cannot be early-stopped based on the available computational resources. For these reasons, this article proposes using a simple conditional gradient algorithm primarily based on closed-form expressions and simple operations: the FWA [20].

In simple terms, the FWA starts at a feasible point and then advances in the direction of a vertex of the feasible set that minimizes the current gradient of the cost function. The step size for moving in the new direction can be determined in various ways; however, in this work, the simplest option is used, as it has a closed-form expression that can be easily evaluated. The algorithm starts at a feasible point $\boldsymbol{U}^0$. Then, at each tth iteration, the following optimization problem is solved:

$$\boldsymbol{\zeta}^t \in \underset{\boldsymbol{U}\in\mathbb{C}_{\mathbb{U}}}{\operatorname{argmin}} \ (\boldsymbol{\zeta}^t)^{\top}\nabla J\left(\boldsymbol{U}^{t-1}\right) \tag{11}$$

where $\nabla J(\boldsymbol{U}^{t-1}) = 2\boldsymbol{Q}\boldsymbol{U}^{t-1} + 2\boldsymbol{\Theta}$. Notice that, if the jth element of $\Lambda^t = \boldsymbol{Q}\boldsymbol{U}^{t-1} + \boldsymbol{\Theta}$ is nonnegative, the jth element of $\boldsymbol{\zeta}^t$ (i.e., $\boldsymbol{\zeta}_j^t$) is equal to $-\eta$, whereas, if negative, $\boldsymbol{\zeta}_j^t = \eta$. Once $\boldsymbol{\zeta}^t$ is calculated, the solution is updated as

$$\boldsymbol{U}^t = (1-\gamma)\,\boldsymbol{U}^{t-1} + \gamma^t\boldsymbol{\zeta}^t \tag{12}$$

where the step size γ^t is defined as $\gamma^t = 2/(t+2)$. This process is repeated for $\texttt{N}_{\texttt{iter}}$ iterations, which is a parameter defined by the designer. Finally, to keep the initial radius of the SDA small, a convenient initial candidate $\boldsymbol{U}_{\text{sq}}$ is calculated following the same procedure as described in [5], where $\boldsymbol{U}_{\text{sq}}$ is obtained by

quantizing $\boldsymbol{U}_{\text{bc}}$ to the closest element in $\mathbb{U}$ and then modifying the vector to meet (3d) and (3e).

V. Simulation Analysis

The system studied is the MVHP grid-connected converter depicted in Fig. 1, with the parameters used in [9] and specified as $S_{\text{nom}} = 9$ MVA, $V_g = 3150$ V (rms), $I_{\text{nom}} = 1649.6$ A (rms), $V_{\text{dc}} = 4840$ V, $R = 0.3$ m Ω, $R_g = 27.51$ mΩ, $L = 350$ μ H, $L_g = 875.6$ μH, $R_c = 4$ m Ω, and $C = 420$ μF. The filter resonances are located at 262 and 491 Hz, the control period is $T_s = 25$ μs, and the system nominal frequency is $f_g = 50$ Hz. Because of long-prediction horizons clearly improving the steady-state performance of MFCS-MPC for high-order systems [3], in all cases the prediction horizon considered was $\mathcal{S} = \{1, 4, 4, 4, 4\}$ (i.e., the size of the N steps were, in order, $\{T_s, 4T_s, 4T_s, 4T_s, 4T_s\}$), with the weighting factors being scaled with the corresponding elements of $\mathcal{S}$ [14]. When comparing the proposed strategy with MFCS-MPC, the following optimization problem is solved by MFCS-MPC:

$$\min_{\boldsymbol{U}(k)} J = \sum_{\ell=k+1}^{k+N} \|\Delta \boldsymbol{y}^{\star}(\ell)\|^2_{\boldsymbol{\lambda}^y_\ell} + \lambda_u \sum_{\ell=k}^{k+N-1} \|\Delta \boldsymbol{u}_{abc}(\ell)\|_2^2$$

s.t. (3a)–(3f)

where $\Delta \boldsymbol{y}^{\star}(\ell) = \boldsymbol{y}^{\star}(\ell) - \boldsymbol{y}(\ell)$ and $\Delta \boldsymbol{u}_{abc}(\ell) = \boldsymbol{u}_{abc}(\ell) - \boldsymbol{u}_{abc}(\ell-1)$. Notice that constraint (3e) is not part of the standard MFCS-MPC formulation, so it is only added when specified. The prediction horizon and sampling period used are the same as those of the proposed OPP-MFCS.

A. SDA Exploration Pattern

The naive circular shift that always locate the initial incumbent as the first explored path, and implemented through the novel generalized exploration pattern matrix, is tested to verify its effectiveness in reducing the number of nodes explored to find the solution. A total of 5601 cases were generated by simulating the system during seven fundamental cycles, where the problem solved at each control period was stored.

Recall that the algorithm finishes when no more nodes are left to explore, or the node limit is reached. Therefore, the algorithm generally keeps exploring nodes after the solution is found. The algorithm was never stopped by node limit during this analysis, so the problem was always solved optimally.

The probability mass function (PMF) of the explored nodes, in percentage, is shown in Fig. 4. As shown, the proposed approach, in general, decreases the number of explored nodes required to find the solution, with its PMF having a shorter tail and all marked percentiles concentrated at smaller numbers. In 67.5% of the cases, the proposed approach explored fewer nodes, whereas in 85%, it explored fewer or the same number of nodes.

These results prove that the proposed approach reduces the maximum number of explored nodes that can early-stop the execution of the SDA. This is the main goal, as this limit defines the computational burden of the SDA. One key benefit of the proposed exploration pattern is the possibility of starting the SDA from level $j = 3N$ in the search tree, as the first path is the initial incumbent [16]. In all cases where the nodes required to find the solution are nonzero, this initialization reduces in $3N = 15$ the number of nodes explored. This leads the proposed exploration pattern to perform better than the traditional pattern in 69.4% of the cases and better or equally in 87%. Even though this might seem like a small improvement, $3N$ fewer nodes can be a considerable number when early stopping the SDA.

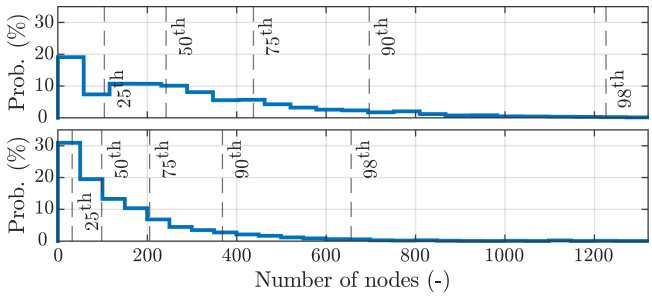

Fig. 4. PMF and percentiles of the nodes explored by the SDA. Upper plot: conventional exploration pattern. Lower plot: proposed approach.

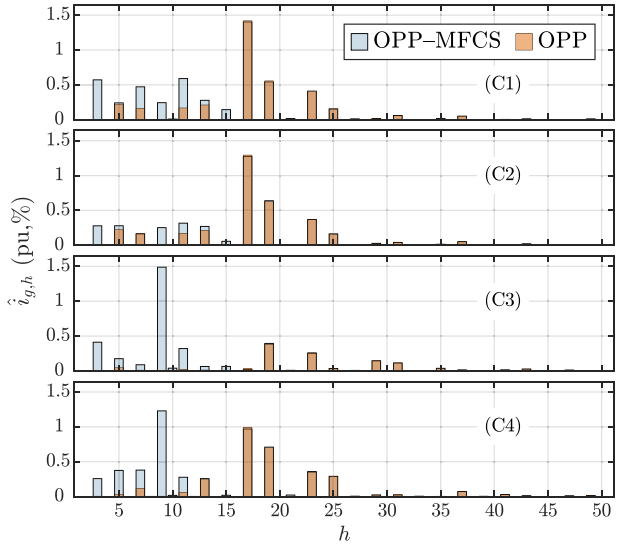

Fig. 5. Fourier spectrum of a grid current for different operating conditions. Comparison between OPP-MFCS and OPPs.

B. Steady-State Performance and OPP Comparison

Four steady-state cases were executed to verify the capability of OPP-MFCS MPC in generating periodic and symmetrical three-phase voltages, using $d = 5$, i.e., $f_{\text{sw}} = 250$ Hz. The cases are as follow: (C1) $p^{\star} = -0.6$, $q^{\star} = 0.2$; (C2) $p^{\star} = 1$, $q^{\star} = 0$; (C3) $p^{\star} = 0$, $q^{\star} = -1$; and (C4) $p^{\star} = 0.8$, $q^{\star} = -0.8$. The Fourier spectra of one grid current are plotted for each case with a granularity of 25 Hz, i.e., the harmonic components are $\mathcal{H} = \{1.5, 2, 2.5, \ldots, 49.5, 50\}$. The results from directly applying the corresponding OPPs are shown alongside the OPP-MFCS results for comparison, to visualize the impact of incorporating them into the MFCS-MPC strategy, and analyze the effect of quantization. The results presented in Fig. 5 show

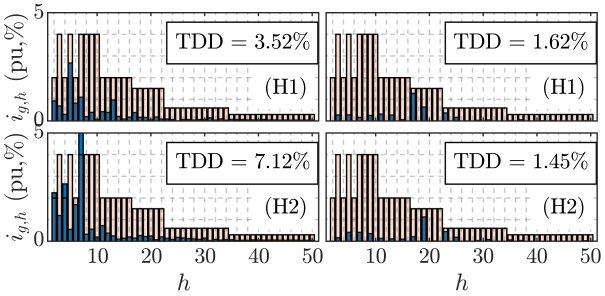

Fig. 6. Fourier spectra comparison between both control strategies in simulation. Left: MFCS-MPC. Right: Proposed OPP-MFCS controller.

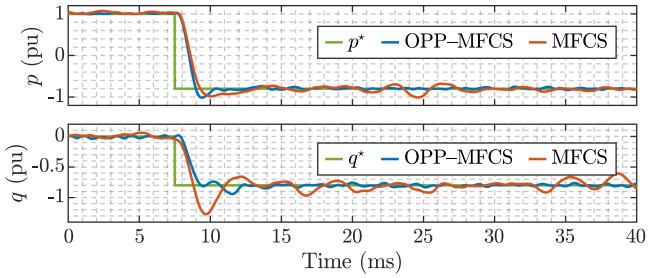

Fig. 7. OPP-MFCS and MFCS-MPC step-response comparison.

that in all cases the respective Fourier spectrum is discrete. Small interharmonics exist in some cases, originating from slight deviations from the original OPP due to the discrete nature of MFCS-MPC. This introduces small quantization errors. The discrete spectra obtained by the proposed strategy are a key improvement over traditional MFCS-MPC, and result from the periodic and approximately three-phase-symmetric voltages obtained in steady-state operation. However, due to quantization error, some low-order harmonics appear, and others increase their amplitude.

A remark is made regarding triplen harmonics. The simple fact of sampling the OPPs leads to small differences in the patterns of the three phases, causing the triplen harmonics to exhibit slightly different amplitudes and phases. Since the common-mode voltage of the OPPs was not minimized during its calculation, these triplen harmonics have large amplitudes, hence, small differences can still cause noticeable unbalanced triplen-harmonics currents. Reducing the amplitude of the OPP's common-mode harmonic components is beyond the scope of this article, thus, it was not part of the OPP calculation. However, this can be included by defining upper bounds for the amplitudes of triplen harmonics, just as it is done for the rest of components considered in the grid codes. It can also be done by adding the square of their amplitudes as extra terms in the cost function of the problem, minimizing the amplitudes together with the grid current TDD. In the same line, the sampling of OPPs naturally leads to an increment on the grid currents TDD. However, that increment is, in general, small. For example, for nominal power and unity power factor (C2), the said TDD is 1.55% when operating with the original OPPs, while it is 1.62% for OPP-MFCS, with a difference of only 0.07% in terms of absolute percentage. Moreover, in all four cases the TDD was small [(C1) 1.89%, (C2) 1.62%, (C3) 1.67%, (C4) 1.91%], and compliant with grid codes requirement. In any case, attenuating the impact on power quality caused by OPP sampling is an important topic and is suggested as future research.

Finally, the steady-state performance of traditional MFCS-MPC [without constraint (3e)], with the proposed OPP-MFCS are compared, for two operating points (H1) $p^\star = 1, q^\star = 0$, and (H2) $p^\star = q^\star = -0.8$, with both strategies operating at $f_{\text{sw}} =$ 250 Hz. Fig. 6 illustrates the results. It can be seen MFCS-MPC only meets the grid code requirements in the (H1) scenario, while in (H2) both TDD and harmonics amplitudes are above the permitted limits. On the other hand, the proposed OPP-MFCS meets all limits defined by grid codes in both scenarios, showing a significantly reduction, in both cases, in the grid current TDD and harmonic amplitudes. Note also that the Fourier spectra are discrete for the proposed strategy. These results suggest OPP-MFCS achieves all steady-state control objectives.

C. Dynamic Response

OPPs are designed for steady-state operation, and their direct application would result in a slow dynamic response. Thus, it is essential to evaluate the impact of combining OPPs with MFCS-MPC, along with the reduced switching frequency of the semiconductors on the dynamic response. To this end, the system is initialized with $p^\star = 1$ and $q^\star = 0$, followed by simultaneous steps on active and reactive power references, leading to $p^\star = -0.8$ and $q^\star = -0.8$. OPP-MFCS operating at $f_{\text{sw}} =$ 250 Hz was compared with MFCS-MPC adjusted approximately for the same switching frequency. Both strategies included the constraint (3e) in the MPC optimization problem to prevent the switching frequency from spiking right after step in the references. For OPP-MFCS, $\hat{c}_\chi(k) = c_{\tilde{u},\chi} + |\tilde{u}_\chi(k) - u_\chi(k-1)|$, while for MFCS-MPC, $\hat{c}_\chi(k)$ was set constant to $\hat{c}_\chi(k) = 3$, which was adjusted so the additional commutations are similar in both strategies. With this constraint a hard limit is posed over the predicted commutations, regulating excessive switching during transients. The prediction horizon was set as $\mathcal{S} = \{1, 4, 4, 4, 4\}$ and $T_s = 25\ \mu$s, with a total of 425 μs.

The instantaneous powers are shown in Fig. 7, whereas the behavior of the system outputs with OPP-MFCS in Fig. 8. As shown, the proposed strategy is as fast and has considerably smaller overshoots than MFCS-MPC, preserving the strongest feature of MFCS-MPC. In addition, it can be seen how the trajectory references of the outputs are quickly tracked.

Regarding the actuation, depicted in Fig. 9, the steady-state pattern is quickly reached with only a few additional switching transitions during the transient, as can be seen in the close-up view presented in Fig. 10. These results also verify the effectiveness of constraint (3e) in reducing the additional commutations during transients. It is important to note that, based on the results in [13], it is expected that additional short pulses could be removed by penalizing the switching transitions in the cost function. Thus, combining the cost functions from [13] and the one currently used may yield a better performance. A deep analysis of the cost function is beyond of the scope of this work and is reserved for future research.

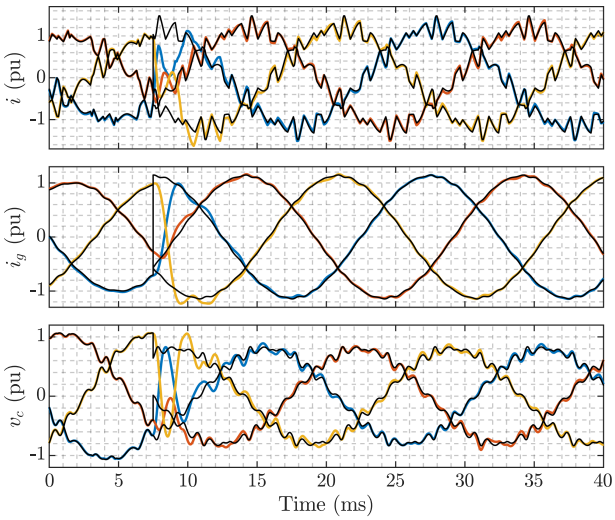

Fig. 8. Dynamic behavior of the system outputs when using OPP-MFCS. Black lines correspond to the steady-state trajectories obtained with OPPs.

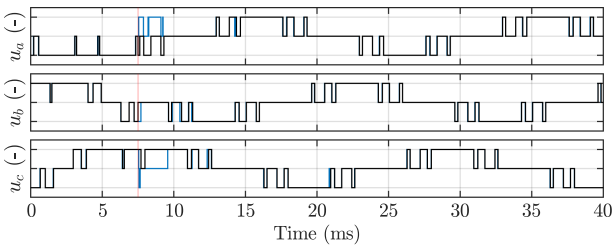

Fig. 9. OPP-MFCS switching patterns during step response. The original OPP patterns are depicted in black lines.

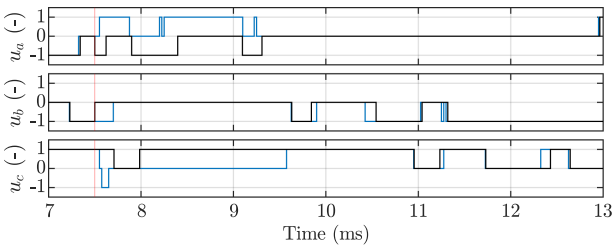

Fig. 10. Close-up view of OPP-MFCS switching patterns during step response. The original OPP patterns are depicted in black lines.

D. SDA Initial Solution

Another benefit of OPP-MFCS concerning SDA efficiency is that $\tilde{\boldsymbol{U}}(k)$ can serve as the initial incumbent for the SDA, provided it meets constraint (3d). When feasible, the term J_u in the cost function becomes zero, potentially leading to a significant reduction in the initial radius of the sphere. In addition, as $\tilde{\boldsymbol{U}}(k)$ is the sampled OPP, it is the steady-state solution of the MFCS problem, directly initializing the SDA with the solution. The proposed initialization method is straightforward: $\boldsymbol{U}_{\text{sq}}$ is used when the FWA is required. Otherwise, every time $\tilde{\boldsymbol{U}}(k)$ is feasible, the SDA is initialized with it; if not, the traditional educated guess is used.

This procedure is different from evaluating the cost function for both options and selecting the one with the lower cost, which requires the computational burden of evaluating two full-depth paths in the search-tree.

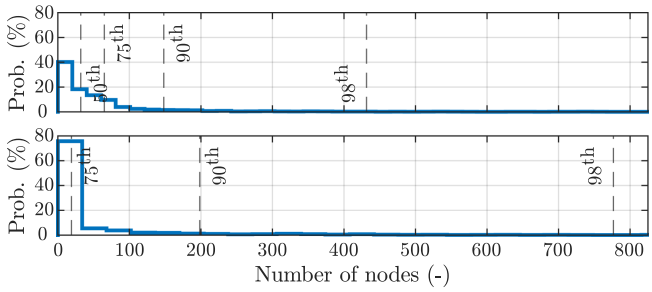

Fig. 11. PMF and percentiles of nodes explored by the SDA. Upper plot: initialization with educated guess. Lower plot: proposed initialization.

The initialization strategy was tested by solving 5601 cases using the proposed exploration pattern and comparing the nodes explored using both the traditional educated guess and the proposed initialization. The PMF histograms, in percentage, are shown in Fig. 11. For the proposed initialization, in 74% of the cases explored zero nodes, meaning the strategy starts the algorithm with the solution. In contrast, for the traditional educated guess, this occured only in 27% of the cases. The PMF for the proposed strategy is primarily concentrated toward the origin, indicating that in the vast majority of cases the number of nodes explored is really low. However, it has a longer tail due to a few instants during transient behavior. This can, however, be mitigated by tightening the condition for when the FWA is used. Although this may lead to occasional small losses in optimality during transients, it would significantly reduce the computational burden overall. This reduction is proved by the fact that the same or fewer nodes were explored with the proposed initialization in 87.07% of the cases (with 62.04% requiring fewer nodes).

VI. Real-Time Implementation and Tests

A thorough computational burden analysis was done employing the software Vitis HLS, whereas the performance of OPP-MFCS was evaluated via HIL experiments.

A. High-Level Synthesis

For the HLS analysis, the controller parameters were set so the resulting computational requirements of the strategy would fit in a commercial FPGA, while still obtaining the steady-state performance shown in Section V-B. This implies reducing the amount of operations required by the controller, while still obtaining sampled OPPs in steady state. This procedure results in a slower dynamic response, as it requires reducing the number of harmonic components used to generate the trajectory references, and, more importantly, reduces the limit for nodes explored, which significantly impact the transient behavior. However, implementing the strategy via HLS provides the worst-case computational resources, meaning that considerable improvements in terms of implementation efficiency are possible.

Thus, the prediction horizon was set as $N = 5$ with three SDAs running in parallel. The number of harmonics used for

TABLE I
FPGA UTILIZATION AND COMPUTATION TIME OF OPP-MFCS MPC

Section	BRAM	DSP–s	FF	CLUT	Time (μs)
Pre–process	3	36	5646	11931	2.51
$\tilde{\boldsymbol{U}}(k)$ generation	0	5	743	1053	0.49
$\tilde{\boldsymbol{Y}}(k)$ generation	1	45	3395	3228	4.08
Pre–FWA	0	54	2814	4917	1.26
$\bar{\boldsymbol{U}}_{\text{unc}}$ generation	0	15	1310	1453	0.33
FWA	0	14	525	4078	2.94
Exp. pattern gen.	0	0	1419	1915	0.23
$\boldsymbol{U}_{\text{ini}}$ calculation	0	0	35	641	0.11
SDA	0	51	28839	22176	9.75
Total	4	220	44726	51392	21.7
Total (%)	2.9	100.0	42.0	96.6	86.8

the reference generator were $H_r^i = 34$, $H_r^c = H_r^g = 0$ (where H_r^i is for the converter currents, H_r^c for the capacitors voltages and H_r^g for the grid currents). The trajectory references for the capacitor voltages and grid currents were approximated by their fundamental components (i.e., $H_r^c = H_r^g = 0$), as it was observed that such approximations were sufficient for OPP-MFCS to achieve the desired steady-state performance. For the FWA, the iterations were set at 20, and each SDA had a limit of 20 nodes explored. This low node limit is achievable only because of the proposed efficient implementation. This not only enhances the overall efficiency of the SDA but also saves exploring 15 nodes by starting the algorithm from the last level, which is significant compared to the limit used.

The implementation was synthesized using the Vitis HLS tool with a 25 μs control period, assuming a Xilinx XC7Z020 Zynq-7000 FGPA, a standard low-cost FPGA [21], featuring 220 DSP slices (DSP-s) (with a single 25×18 bit multiplier), 53 200 LUTs for combinatorial operations (CLUT), 106 400 FFs, and 140 BRAM. Besides the SDA, the whole controller was implemented using a 100 MHz clock and fixed-point arithmetic, where 18-b words were used for all variables that are not integers, as it allows multiplications to be executed by a single DSP-s [21]. For integers, in general, shorter words were used depending on the values the variable can take. For the SDA, a clock of 200 MHz was used, and to set the word lengths, a testbench with 3900 cases was run, adjusting the lengths to ensure the exact solution was obtained in all cases. With that configuration, the worst elapsed time per SDA was 9.75 μs. All `sine` and `atan2` functions were implemented usign LUTs to reduce the computation time and the DSP-s required. In addition, the control strategy was divided into sections executed sequentially (worst case).

The summary of the resource usage per section is presented in Table I. From Table I, it is important to highlight the low computational burden of the FWA, which allows solving (10) in a time- and resource-efficient manner, allowing MFCS-MPC to be viable in real time, even during transients [5]. These results confirm that OPP-MFCS can run in real time on a commercial control platform, as the worst-case scenario of resources required and computation time are within limits.

B. Hardware-in-the-Loop

The proposed control strategy was tested using an OPAL-RT real-time simulator in a HIL configuration. The model used was an OP4510 with an OP4520 expansion unit. The OP4510 is equipped with a Xilinx FPGA of the Kintex 7 family and an Intel Xeon E3-1240 V6 Quad-Core @3.7 GHz processor unit. The system's real-time simulation ran on the platform's FPGA using the eHSx64 electrical solver. The real-time execution of the controller is done in the processor of the OP4510, running at a control period of 25 μs. The measurements, coming from the analog outputs of the OP4520, are fed to the processor through the analog inputs of the OP4520. The control actions, which are the gating signals of the semiconductors, are taken out from the processor using the digital outputs and are fed to the eHSx64 solver using the digital inputs.

The parameters were set exactly as in the HLS analysis, with the only difference being that the SDA was not parallelized, due to the fixed architecture of the processor unit, so a node limit of 60 was used to achieve a similar performance as in the HLS analysis. With the main objective of assessing the impact of incorporating OPPs into the standard MFCS-MPC method, the proposed strategy's steady-state performance was benchmarked against state-of-the-art MFCS-MPC adjusted with the same parameters, to clearly illustrate the benefits of the proposed method. Again, the prediction horizon for both strategies was set as $\mathcal{S} = \{1, 4, 4, 4, 4\}$, with the weighting factors being scaled with the corresponding elements of $\mathcal{S}$ [14], and, to use the standard state-of-the-art MFCS-MPC, the constraint (3e) was not applied to any of the strategies. The OPP-MFCS controller was operated at a switching frequency of 250 Hz.

During the test, significant delays were observed in the measurements, a phenomenon commonly encountered in real systems. This led to large oscillations in the system steady-state behavior with the standard MFCS-MPC, and an extended delay compensation strategy alone was insufficient to fix the problem. To solve it without adding any additional elements to the control loop, it was necessary to extend the delay compensation and increase the switching frequency of MFCS-MPC to ensure proper tracking of the references and a performance close to what is demanded by grid codes. Therefore, the weighting factor λ_u was adjusted to obtain an approximate switching frequency of 600 Hz. On the other hand, for the OPP-MFCS strategy, the only necessary modifications were the same extended delay compensation and an increase in λ_ℓ^u to regulate the aggressiveness of the response. This ensured the desired steady-state performance. It was not necessary to use a pattern with a higher switching frequency to meet the grid codes.

The steady-state comparison between the two strategies is presented in Fig. 12 for the operation points (H1) $p^\star = 1$, $q^\star = 0$, and (H2) $p^\star = q^\star = -0.8$. The grid code is verified by including the limits for TDD (5%) and current harmonics defined by the IEEE Std. 519-2022 [1]. From the Fourier spectra of the grid current, it is observed that the MFCS-MPC strategy meets the harmonic limits only in one of the cases, but fails to comply with the maximum TDD in both. In contrast, the proposed OPP-MFCS strategy achieves both goals in both cases. Regarding TDD, it is not only below 5% but also significantly smaller than that of MFCS-MPC, getting a reduction of more than 70%. Note that, in case (H1), as seen in simulation, some even and triplen harmonics appear in the grid currents. This is

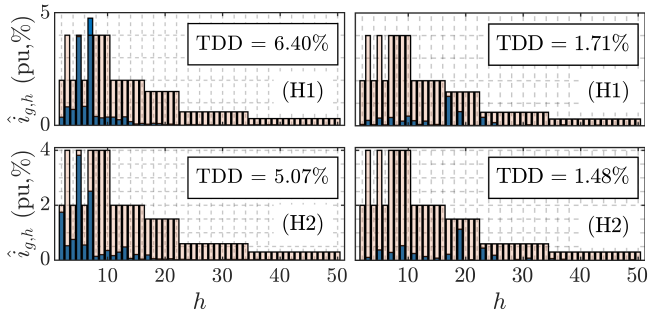

Fig. 12. Fourier spectra comparison between both control strategies in HIL tests. Left: MFCS-MPC. Right: Proposed OPP-MFCS controller.

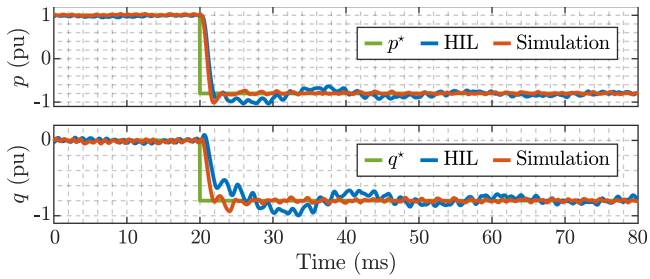

Fig. 13. HIL and simulation step response comparison.

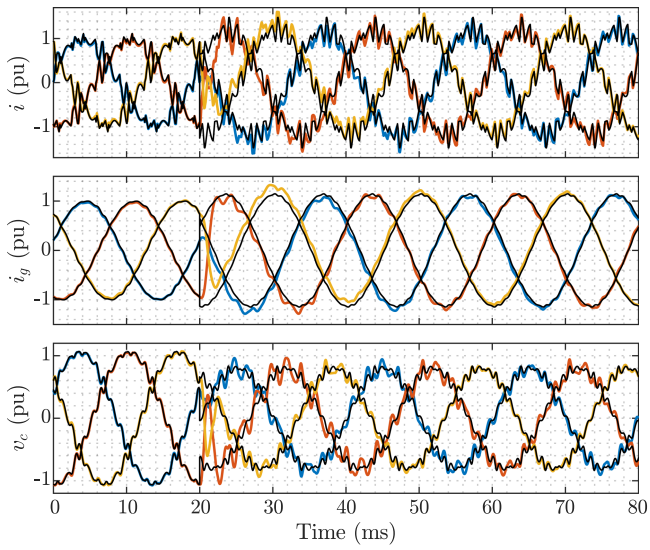

Fig. 14. Step response during HIL test. Black lines correspond to the steady-state trajectories obtained with OPPs.

attributed to measurement delay causing tracking error, which the controller compensates by barely modifying the steady-state pattern, resulting in a slight loss of the symmetry between the three phases and the pattern's quarter- and half-wave symmetry. However, the amplitudes are negligible and smaller than the limit defined by the grid codes in all cases.

The step response transitioning between those two operation points was compared to simulation results for the same horizon, where the OPP-MFCS problem was always solved to optimality. Figs. 13 and 14 show the dynamic behavior of active and reactive power, as well as the system outputs. Although both responses

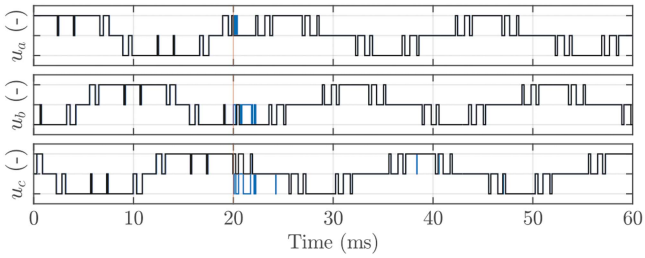

Fig. 15. OPP-MFCS switching patterns during step response in HIL test. Black lines depict the original OPPs.

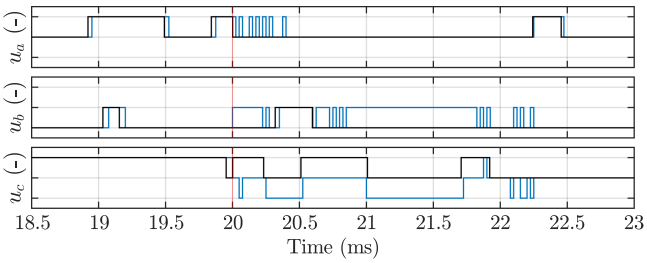

Fig. 16. Close-up view of OPP-MFCS switching patterns during step response in HIL test. Black lines depict the original OPPs.

are fast, the high value of λ_ℓ^u and the low limit for explored nodes caused the response to be slower and to exhibit oscillations in power, resulting from the interaction of the unidirectional currents and the grid voltage. Recall that transitory unidirectional currents appear because of the natural response of the filter. Moreover, the small node limit used for the SDA required increasing λ_ℓ^u to reduce the strategy's sensitivity to suboptimal solutions and ensuring that the steady-state patterns closely match the OPPs. Thus, the loop speed was reduced.

On the other hand, the switching patterns of the converter are presented in Fig. 15, with a close-up view in Fig. 16. It can be seen how the steady-state patterns are quickly reached. However, immediately after the step, a large number of additional pulses are added. This demonstrates the effectiveness of the proposed constraint (3e) in limiting additional switching transitions, a feature not included in standard MFCS-MPC formulation.

The various tests and results above have assessed the proposed OPP-MFCS strategy. It showed satisfactory performance despite the low number of nodes explored, showing the benefits of the proposed improvements, and confirming and concluding that all the control objectives outlined in Section II-B were successfully met.

VII. Conclusion

This work addresses the main weaknesses of MFCS-MPC and aims to make it suitable for grid-connected applications, specifically LCL-filter grid-connected MVHP converters, where multiple control objectives must be achieved simultaneously. By combining the strengths of MFCS-MPC with the performance benefits of OPPs, the proposed OPP-MFCS strategy meets grid codes, while operating at a fixed, low switching frequency with periodic and approximately three-phase symmetric voltages,

while still providing a fast dynamic response. To maintain real-time viability, this work proposed several efficiency enhancements for the SDA. A generalized exploration pattern for the SDA's search-tree and an SDA initialization based on OPPs were introduced. In addition, the FWA was implemented to enable transient operation. All the contributions were tested through simulation and HIL experiments, along with a computational burden analysis. The results confirmed that the proposed strategy meets all control objectives while complying with the grid connection requirements stated in the IEEE Std. 519-2022.

Future research activities to further enhance the strategy include: developing an approach for the tuning of the weighting factors in the cost function; alleviate the impact of sampled OPPs on common-mode harmonics; evaluating alternative approaches to manage the number of additional switching transitions during transients; implementing MFCS-MPC using industrial hardware; and addressing other grid issues, such as ensuring compliance with grid codes during frequency variations.

REFERENCES

[1] *IEEE Standard for Harmonic Control in Electric Power Systems*, IEEE Std 519-2022, Aug. 2022.

[2] T. Geyer, *Model Predictive Control of High Power Converters and Industrial Drives*. Hoboken, NJ, USA: Wiley, 2016.

[3] P. Karamanakos, E. Liegmann, T. Geyer, and R. Kennel, "Model predictive control of power electronic systems: Methods, results, and challenges," *IEEE Open J. Ind. Appl.*, vol. 1, pp. 95–114, 2020.

[4] T. Geyer and D. E. Quevedo, "Multistep finite control set model predictive control for power electronics," *IEEE Trans. Power Electron.*, vol. 29, no. 12, pp. 6836–6846, Dec. 2014.

[5] R. Baidya et al., "Enabling multistep model predictive control for transient operation of power converters," *IEEE Open J. Ind. Electron. Soc.*, vol. 1, pp. 284–297, 2020.

[6] P. Karamanakos and T. Geyer, "Guidelines for the design of finite control set model predictive controllers," *IEEE Trans. Power Electron.*, vol. 35, no. 7, pp. 7434–7450, Jul. 2020.

[7] A. Birth, T. Geyer, H. D. T. Mouton, and M. Dorfling, "Generalized three-level optimal pulse patterns with lower harmonic distortion," *IEEE Trans. Power Electron.*, vol. 35, no. 6, pp. 5741–5752, Jun. 2020.

[8] T. Geyer, N. Oikonomou, G. Papafotiou, and F. D. Kieferndorf, "Model predictive pulse pattern control," *IEEE Trans. Ind. Appl.*, vol. 48, no. 2, pp. 663–676, Mar./Apr. 2012.

[9] T. Dorfling, H. D. T. Mouton, and T. Geyer, "Generalized model predictive pulse pattern control based on small-signal modeling—Part 1: Algorithm," *IEEE Trans. Power Electron.*, vol. 37, no. 9, pp. 10476–10487, Sep. 2022.

[10] T. Geyer and N. Oikonomou, "Model predictive pulse pattern control with very fast transient responses," in *Proc. IEEE Energy Convers. Congr. Expo.*, Sep. 2014, pp. 5518–5524.

[11] S. Rahmanpour, P. Karamanakos, and T. Geyer, "Three-level optimized pulse patterns for grid-connected converters with LCL filters," in *Proc. IEEE Energy Convers. Congr. Expo.*, 2023, pp. 1430–1437.

[12] R. P. Aguilera et al., "Selective harmonic elimination model predictive control for multilevel power converters," *IEEE Trans. Power Electron.*, vol. 32, no. 3, pp. 2416–2426, Mar. 2017.

[13] C. González, A. Angulo, and F. Mancilla-David, "Enhancing multistep finite control set performance of 3L-NPC converters using optimal pulse patterns," in *Proc. IECON-47th Annu. Conf. IEEE Ind. Electron. Soc.*, Oct. 2021, pp. 1–6.

[14] C. González and A. Angulo, "Multistep-finite-control-set model predictive control with variable-step prediction horizon," in *Proc. IEEE 8th Southern Power Electron. Conf. 17th Braz. Power Electron. Conf.*, 2023, pp. 1–8.

[15] T. Dorfling, H. du Toit Mouton, T. Geyer, and P. Karamanakos, "Long-horizon finite-control-set model predictive control with nonrecursive sphere decoding on an FPGA," *IEEE Trans. Power Electron.*, vol. 35, no. 7, pp. 7520–7531, Jul. 2020.

[16] P. Karamanakos, T. Geyer, T. Mouton, and R. Kennel, "Computationally efficient sphere decoding for long-horizon direct model predictive control," in *Proc. IEEE Energy Convers. Congr. Expo.*, Sep. 2016, pp. 1–8.

[17] E. Zafra, S. Vazquez, A. M. Alcaide, J. I. Leon, and L. G. Franquelo, "Alternate search pattern for parallel sphere decoder in long prediction horizon FCS-MPC," *IEEE Trans. Ind. Electron.*, vol. 71, no. 7, pp. 8185–8189, Jul. 2024.

[18] E. Zafra et al., "Parallel sphere decoding algorithm for long-prediction-horizon FCS-MPC," *IEEE Trans. Power Electron.*, vol. 37, no. 7, pp. 7896–7906, Jul. 2022.

[19] K. Vogklis and I. Lagaris, "BOXCQP: An algorithm for bound constrained convex quadratic problems," in *Proc. 1st Int. Conf. From Sci- entific Comput. Comput. Eng.*, 2004, pp. 1–8.

[20] M. Jaggi, "Revisiting Frank-Wolfe: Projection-free sparse convex optimization," in *Proc. 30th Int. Conf. Mach. Learn.*, Jun. 2013, pp. 427–435. [Online]. Available: https://proceedings.mlr.press/v28/jaggi13.html

[21] T. Dorfling, H. D. T. Mouton, and T. Geyer, "Generalized model predictive pulse pattern control based on small-signal modeling—Part 2: Implementation and analysis," *IEEE Trans. Power Electron.*, vol. 37, no. 9, pp. 10488–10498, Sep. 2022.

Cristóbal González (Student Member, IEEE) was born in Temuco, Chile, in 1994. He received the B.Sc. and M.Sc. degrees in electrical engineering from the Universidad Técnica Federico Santa María (UTFSM), Valparaíso, Chile, in 2017 and 2023, respectively. He is currently working toward the Ph.D. degree with the Electromechanics and Power Electronics Group, Eindhoven University of Technology, Eindhoven, The Netherlands.

His research interests include optimal control strategies, control of grid-connected converters, and multilevel converters.

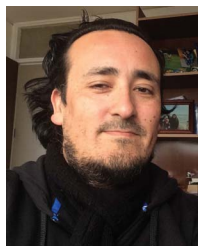

Alejandro Angulo (Member, IEEE) was born in Osorno, Chile. He received the B.Sc. and M.Sc. degrees in electrical engineering from the "Universidad Técnica Federico Santa María" (UTFSM), Valparaíso, Chile, in 2004 and 2007, respectively, and the Ph.D. degree in operational research from "Universidad de Chile," Santiago, Chile, in 2015.

He is currently an Assistant Professor with the Department of Electrical Engineering, UTFSM. His main research interests include integer programming, optimization applied to power converters control, model predictive control, optimization algorithms for embedded systems, and large-scale optimization applied to power system operation and planning.

Fernando Mancilla-David (Member, IEEE) was born in Valparaíso, Chile. He received the B.S. degree in electrical engineering from the "Universidad Técnica Federico Santa María," Valparaíso, Chile, in 1999 and the M.S. and Ph.D. degrees in electrical engineering from the University of Wisconsin-Madison, Madison, WI, Wisconsin, in 2002 and 2007, respectively.

Since 2007, he has been with the Department of Electrical Engineering, University of Colorado Denver, Denver, CO, USA, where he is currently a Full Professor. He has been a visiting scholar with several research institutions around the world, including ABB Corporate Research, Västerås, Sweden, "CentraleSupélec," Paris, France, "Technische Universität Berlin," Berlin, Germany, "Università degli studi Roma Tre," Rome, Italy, "Universidade Federal de Pernambuco," Recife, Brazil, "Universitat Politècnica de Catalunya," Barcelona, Spain, ITMO University, Saint Petersburg, Russia, "Universidad Técnica Federico Santa María," Valparaíso, Chile, and ITAM University, Mexico City, Mexico. During 2016–1017 academic year, he was a Fulbright Scholar on sabbatical leave with PUC-Rio University, Rio de Janeiro, Brazil. His research interests are power system analysis, energy systems, utility applications of power electronics, control systems, and optimization problems.